






Subsolar-mass binary mergers of strange stars and neutron stars: gravitational waves and ejecta

Yong Gao ^{1,*} Ming-Zhe Han ^{1,2} Kenta Kiuchi ^{1,3} Masaru Shibata ^{1,3} Enping Zhou ⁴ and Kenta Hotokezaka ^{5,1}

¹Max Planck Institute for Gravitational Physics (Albert Einstein Institute), 14476 Potsdam, Germany

²Key Laboratory of Dark Matter and Space Astronomy, Purple Mountain Observatory,
Chinese Academy of Sciences, Nanjing, 210033, People's Republic of China

³Center of Gravitational Physics and Quantum Information,
Yukawa Institute for Theoretical Physics, Kyoto University, Kyoto, 606-8502, Japan

⁴School of Physics, Huazhong University of Science and Technology, Wuhan 430074, China

⁵Research Center for the Early Universe, Graduate School of Science,
The University of Tokyo, Bunkyo, Tokyo 113-0033, Japan

(Dated: July 9, 2026)

We present the first numerical-relativity simulations of subsolar-mass binary strange star (SS) mergers and compare with binary neutron star (NS) mergers across equations of state, masses, and mass ratios. The self-bound nature of SSs makes them less deformed during the inspiral and keeps a sharp surface up to contact, driving strong shock heating and a large radial bounce that are far weaker in the NS. The more compact SS thus reaches a higher gravitational-wave cutoff frequency f_{cut} before contact but a lower post-merger peak frequency f_2 . Within each class these frequencies follow quasi-universal relations with the tidal deformability, and their ratio f_2/f_{cut} cleanly separates the two classes. Both classes can eject $\sim 10^{-2} M_{\odot}$ of material, neutron-rich for the NS and decompressed quark matter for the SS, a potential source of an electromagnetic counterpart whose observation could test the SS and NS hypotheses for subsolar-mass events.

Introduction—The LIGO–Virgo–KAGRA (LVK) network has now catalogued over 300 compact-binary coalescences [1, 2]. The vast majority are binary black holes (BBHs), with two binary neutron star (BNS) events [3, 4] and three confident neutron-star–black-hole binaries [5, 6]. Every confidently measured component mass lies above $1 M_{\odot}$ [7], consistent with standard stellar evolution. A growing effort is under way to probe the *subsolar* regime. Dedicated pipelines have scanned LVK data from the third and fourth observing runs for subsolar-mass binaries [8–10], and candidate events have surfaced—GW231109_235456 [11] and the O4 alerts S250818k and S251112cm [12, 13]—though none has yet withstood scrutiny as a confident detection. A candidate optical counterpart to S250818k was even identified [14], but follow-up favoured a Type IIb supernova over a kilonova [15, 16].

A subsolar event would point to new physics, such as a primordial black hole [17–23] or an unconventionally formed NS, because standard stellar evolution cannot produce a subsolar NS: both core-collapse supernovae and the accretion-induced collapse of white dwarfs are set by the Chandrasekhar mass, which yields a minimum NS mass of $\sim 1.17 M_{\odot}$ [24, 25], consistent with the lightest measured NS [26] (though see Ref. [27]). Hints of lighter objects nonetheless exist: the mass of the central compact object in the supernova remnant HESS J1731–347 is inferred to be $0.77^{+0.22}_{-0.17} M_{\odot}$ [28].

Subsolar NSs might instead form in gravitationally unstable collapsar disks, where the low electron fraction Y_e of neutron-rich fragments suppresses the local Chandrasekhar mass and allows collapse at subsolar mass [29–32], although for this scenario, an unusually efficient cooling process would be necessary (see also a discussion in [33] for a relevant topic). Alternatively, a subsolar compact star could be a strange star (SS). If strange quark matter—deconfined u , d , and s quarks—is the true ground state of baryonic matter, as conjectured by

Bodmer and Witten [34–37], then SSs are self-bound and not subject to a Chandrasekhar-type collapse threshold, and so extend naturally to subsolar masses. Such low-mass SSs have been proposed to form as relics of the early Universe [35, 38], through the collapse of rapidly rotating NSs [39], or via the accretion-induced collapse of a white dwarf whose core is converted to strange matter [40, 41].

Unlike BHs, NSs and SSs are tidally deformed during the inspiral [43, 44] and can eject matter at merger to power a kilonova [45, 46] (see, e.g., [47, 48] and references therein). The tidal deformation accelerates the inspiral and leaves an imprint on the gravitational-wave (GW) signal, encoded at leading order by the mass-weighted dimensionless tidal deformability $\tilde{\Lambda}$ [49–54]. This signature strengthens steeply toward subsolar masses, with the deformability of an individual star growing from $O(10^3)$ at $1 M_{\odot}$ to $O(10^6\text{--}10^7)$ at $0.1 M_{\odot}$, making the subsolar regime exceptionally sensitive to the equation of state (EOS) [55–57]. Search templates that neglect these matter effects may lose a significant fraction of their sensitive volume [58], while the same imprint already lets current detectors separate a subsolar NS from a BBH [22, 59].

The subsolar regime is, moreover, a promising place to tell a subsolar SS from an NS. An SS is self-bound and compact, whereas an NS is gravitationally bound and extended, and the two evolve in opposite directions toward lower masses. The NS grows more extended, reaching radii $R \sim 11\text{--}14$ km at $M \sim 0.5 M_{\odot}$ and larger still at lower masses, whereas the self-bound SS shrinks as $R \propto M^{1/3}$ to ~ 8 km and below. The SS is thus systematically less deformable, and the two classes follow $\tilde{\Lambda}$ – M relations of markedly different slope (Fig. S1). In principle the inspiral tidal deformability can separate them, but only for very loud signals or by combining many events [60, 61]. A soft-EOS NS and an SS also overlap in $\tilde{\Lambda}$ across a wide range of masses and EOSs, leaving the leading-order tidal signature degenerate. The merger it-

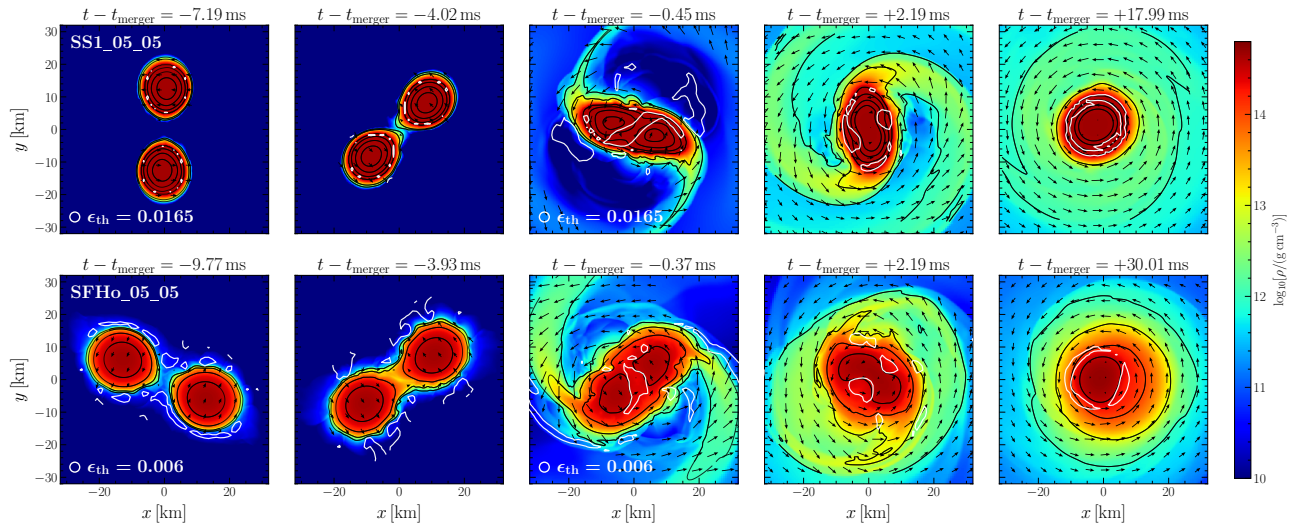


FIG. 1. Equatorial-plane rest-mass density $\log_{10}[\rho/(\text{g cm}^{-3})]$ (colour) for the equal-mass $0.5+0.5 M_{\odot}$ SS (SS1, top row) and NS (SFHo, bottom row) binaries, shown at five times relative to merger $t - t_{\text{merger}}$ (indicated above each panel), from the late inspiral (left) to the post-merger remnant (right). Black curves are rest-mass-density iso-contours at $\log_{10}[\rho/(\text{g cm}^{-3})] = 12, 13, 14.57, 14.59, 14.61, 14.63$ for the SS and 12, 13, 14, 14.5 for the NS. White curves are iso-contours of the thermal part of the specific internal energy, ϵ_{th} , at the value labelled in the first panel of each row (0.0165 for the SS, 0.006 for the NS), tracing the shock-heated contact layer. Arrows show the in-plane coordinate velocity. The compact, self-bound SS is only weakly deformed during inspiral and drives a strong shock and a large radial bounce at contact, whereas the larger, more tidally deformable NS develops pronounced spiral arms and sheds mass before merger; both relax to a rotating remnant surrounded by an extended disk. The animations of the snapshots and corresponding GWs can be found at [42].

self, however, is essentially unexplored in the subsolar regime. We therefore ask how subsolar SS and NS binaries merge—what governs their dynamics, their characteristic merger and post-merger gravitational-wave frequencies, and their mass ejection—and whether these break the inspiral degeneracy between the two classes.

Such simulations remain scarce in the subsolar regime. On the NS side, numerical relativity (NR) has so far treated a binary in which only one of the two components is a subsolar star [59], whereas binary SS mergers have been modelled only at canonical or higher masses, either with smoothed-particle hydrodynamics under the conformal-flatness approximation [62] or in full general relativity [63–65]. The self-bound SS surface is a sharp, near-discontinuous density drop that standard hydrodynamics resolves only with care [66, 67]. In this Letter we present NR simulations of subsolar-mass binary SS mergers for the first time and systematically contrast their dynamics, gravitational-wave spectra, and ejecta with those of subsolar binary NS mergers. Throughout, we use geometric units with $G = c = 1$, where G and c are the gravitational constant and the speed of light, respectively.

Numerical models and grid setup—Each class spans a stiff-to-soft range of EOSs—DD2, SFHo, and WFF1 for the NSs and the (quasi-)MIT-bag family SS1–SS3 [68] for the SSs (Fig. S1)—across component masses $0.3\text{--}0.7 M_{\odot}$ and mass ratios $q = 1, 1.22, \text{ and } 1.5$ (Table S1). We construct the quasi-equilibrium initial data with FUKA [69], augmented with a self-bound surface solver for the SSs. The binaries start at a separation of $\approx 33\text{--}37$ km, with the orbital eccentricity iteratively

reduced to $\lesssim 7 \times 10^{-4}$.

We evolve the fully general-relativistic hydrodynamics with SACRA-K [70], a GPU-accelerated port of SACRA-MPI [71–73], in the moving-puncture Baumgarte–Shapiro–Shibata–Nakamura formulation [74–77] with the Z4c constraint-propagation prescription [78] and fourth-order finite differencing. The hydrodynamics uses a high-resolution shock-capturing scheme—the Harten–Lax–van Leer-contact (HLLC) Riemann solver (cf. the NANASI code [73, 79]) for the NSs and the Harten–Lax–van Leer (HLL) solver for the SSs, whose sharp self-bound surface requires a more numerically robust scheme. Shock heating is captured by a Γ -law thermal component added to each cold EOS, with $\Gamma_{\text{th}} = 4/3$ for the SSs and 1.75 for the NSs. The grid is a box-in-box mesh of ten 2:1 refinement levels, the finest four comoving with each star ($2N \times 2N \times N$ points, equatorial symmetry), evolved at three resolutions (Table S1). The code’s parallel setup and performance are summarized in Table S2. We extract GWs at $r \approx 700$ km and identify the dynamical ejecta with the Bernoulli criterion $-hu_t > 1$, with h the specific enthalpy and u_t the time component of the four-velocity.

Merger dynamics and GW signal.—An SS is self-bound by the strong interaction and of nearly uniform density, whereas an NS is gravitationally bound, centrally condensed, and more extended. This structural difference shapes how the two objects merge, which we illustrate with representative equal-mass $0.5+0.5 M_{\odot}$ SS and NS binaries. The SS (SS1) is more compact: $R \approx 8.4$ km, $C \equiv M/R \approx 0.088$, and dimensionless tidal deformability $\Lambda = 5.2 \times 10^4$, versus 12.4 km, 0.060,

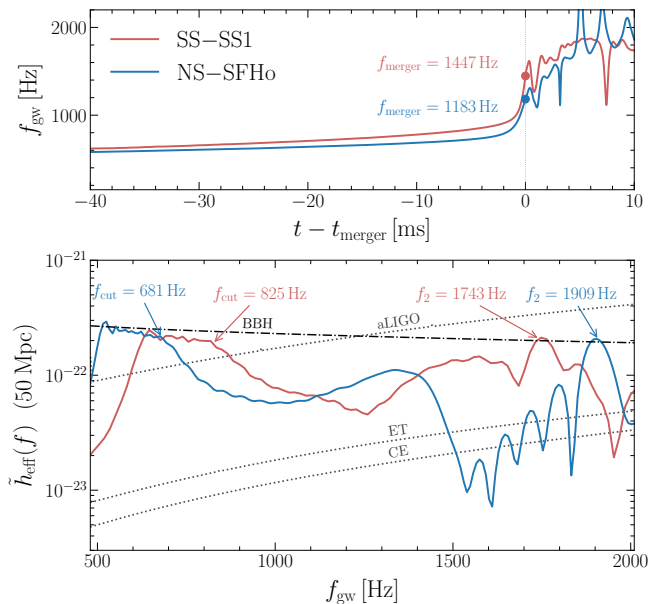


FIG. 2. GW signal from the representative equal-mass $0.5 + 0.5 M_{\odot}$ NS-SFHo (blue) and SS1 (red) binaries. *Top*: instantaneous frequency f_{gw} of the $\ell = m = 2$ mode versus retarded time relative to merger. The filled circles mark the value at the amplitude peak. *Bottom*: effective amplitude $\tilde{h}_{\text{eff}}(f)$ for a source at 50 Mpc, marking the cutoff frequency f_{cut} and the post-merger peak f_2 , with representative detector noise curves (aLIGO, Einstein Telescope, Cosmic Explorer) and a nonspinning binary-black-hole inspiral (BBH) for reference.

and 8.2×10^4 , respectively, for the NS (SFHo). We follow their merger through the rest-mass-density snapshots of Fig. 1 and the GW signal of Fig. 2: the instantaneous GW frequency as a function of retarded time (*top*) and the effective spectrum $\tilde{h}_{\text{eff}}(f)$ for a face-on source at a hypothetical distance of $D = 50$ Mpc (*bottom*).

With the same chirp mass, the two binaries follow the point-particle inspiral almost identically at large separation, where the effective GW amplitude scales approximately as $\tilde{h}_{\text{eff}} \propto f^{-1/6}$. As tidal effects become sizeable in the late inspiral, \tilde{h}_{eff} departs from this nonspinning-BBH baseline and steepens; the break defines the cutoff frequency f_{cut} (lower panel of Fig. 2), which we locate by fitting a broken power law to $\tilde{h}_{\text{eff}}(f)$.

The first column of Fig. 1 shows the density field at f_{cut} . Below this frequency the binary follows a quasi-circular inspiral and radiates strongly; above it tidal effects accelerate the late inspiral off this track and the binary evolves rapidly toward merger, so its GW frequency sweeps up and \tilde{h}_{eff} drops steeply [80]. The more compact SS has smaller tidal deformability, so its cutoff lies higher, $f_{\text{cut}} \simeq 825$ Hz against 681 Hz for the NS. Beyond f_{cut} the two binaries reach merger by different mechanisms. As shown in the second column of Fig. 1, the more compact SS keeps its binary-like structure up to contact and becomes dynamically unstable once the binary reaches the innermost stable circular orbit [81–83]. The more extended NS instead sheds mass through its surface before

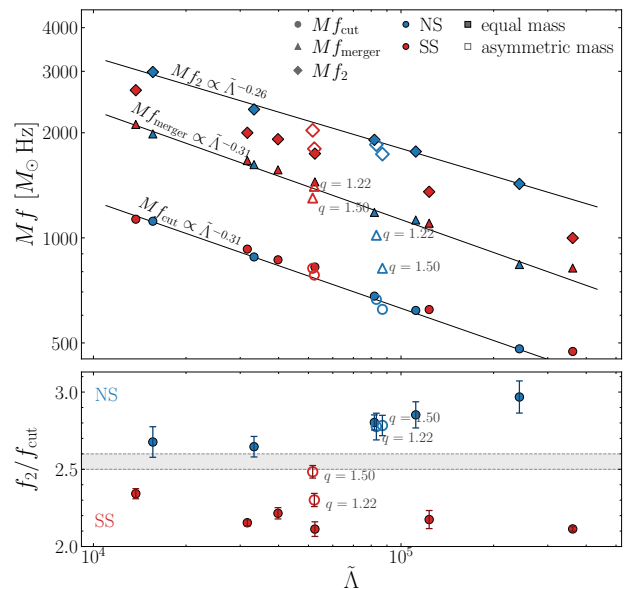


FIG. 3. Characteristic GW frequencies of all binaries in the grid, scaled by the total mass M and plotted against the mass-weighted tidal deformability $\tilde{\Lambda}$. *Top*: cutoff frequency (Mf_{cut} , circles), frequency at the amplitude peak (Mf_{merger} , triangles), and dominant post-merger peak (Mf_2 , diamonds) for NS (blue) and SS (red); filled symbols are equal-mass, open symbols unequal-mass, with the mass ratio q marked next to the corresponding open triangles. Solid lines are power-law fits to the NS sequence (all NSs for f_{cut} , the equal-mass NSs only for f_{merger} and f_2). *Bottom*: the ratio f_2/f_{cut} , which cleanly separates the two classes; the shaded band at $f_2/f_{\text{cut}} = 2.5$ – 2.6 marks the gap between the SS branch (below) and the NS branch (above). Markers use the finest-resolution value. The error bar is the half-spread (max – min)/2 across the three grid resolutions evolved per binary (Table S1).

contact, where its orbital kinetic energy is dissipated.

Because the SS has a smaller tidal deformability and reaches merger at a smaller separation, its GW amplitude peaks at a higher frequency, $f_{\text{merger}} = 1447$ Hz against 1183 Hz for the NS. The merger shown in the third and fourth columns of Fig. 1 is far more violent for the SS. Its self-bound cores collide at higher velocity, and the steep pressure gradient at the contact surface drives a strong shock that heats the layer to a peak thermal energy $\epsilon_{\text{th}} \gtrsim 0.03$, hotter and more sharply confined than in the NS (white ϵ_{th} contours at 0.0165 for the SS against 0.006 for the NS). The shocked double cores then rebound from a compressed contact at ~ 7 km out to $\simeq 14$ km (third column). This large radial bounce raises spiral arms that shed mass at $t - t_{\text{m}} \sim 1$ – 2 ms (fourth column). The NS contact is milder. Being more extended and having a larger tidal deformability, it instead develops pronounced spiral arms already before merger at $t - t_{\text{m}} \sim -2$ ms to -1 ms.

The post-merger remnants then oscillate at the dominant post-merger frequency f_2 for tens of milliseconds and settle into differentially rotating configurations surrounded by extended disks. The angular velocity rises from a slowly rotating core to a maximum at intermediate radii and then declines

outward as in the canonical-mass NS mergers. As shown in the lower panel of Fig. 2, f_2 is lower for the SS, ≈ 1750 Hz against ≈ 1900 Hz for the NS, even though before merger the SS is more compact. This anticorrelation originates from the SS’s large radial bounce and shock re-expansion at merger, which lower the average density of the oscillating remnant.

Quasi-universal relations and discrimination.—The characteristic frequencies described above differ between the two classes, but each also depends on the EOS, mass, and mass ratio, so a single frequency difference is not by itself diagnostic. To disentangle these dependences we span a grid of three EOSs per class, component masses $0.3\text{--}0.7 M_\odot$, and mass ratios $q = 1, 1.22, \text{ and } 1.5$. We then seek quasi-universal relations linking the characteristic GW frequencies f_{cut} , f_{merger} , and f_2 to the mass-weighted dimensionless tidal deformability,

$$\tilde{\Lambda} = \frac{16}{13} \frac{(m_1 + 12m_2)m_1^4 \Lambda_1 + (m_2 + 12m_1)m_2^4 \Lambda_2}{(m_1 + m_2)^5}, \quad (1)$$

the leading-order tidal imprint on the waveform. For canonical-mass NS binaries, f_{merger} and f_2 are known to obey such relations with $\tilde{\Lambda}$, and a departure of the $f_2\text{--}\tilde{\Lambda}$ relation has been proposed as a signature of a strong phase transitions in the remnant [84–87]. We test whether these relations persist in the subsolar regime and how the self-bound SSs depart from them.

Fig. 3 collects the three frequencies, each scaled by the total mass M , against $\tilde{\Lambda}$. We evolved three resolutions per binary (Table S1) and use the finest-resolution value of each frequency in the fits below. The half-spread (max – min)/2 across resolutions is $\lesssim 2.6\%$, $\lesssim 5\%$, and $\lesssim 3.6\%$ for f_{cut} , f_{merger} , and f_2 , respectively, and $\lesssim 3.7\%$ for the ratio f_2/f_{cut} shown as error bars in the lower panel, well below the inter-class differences. We fit f_{cut} to all binaries but f_{merger} and f_2 to the equal-mass binaries only, because in the asymmetric systems the strong tidal force alters the merger dynamics and shifts these frequencies (an effect also found for canonical-mass BNS [88]), as we discuss separately. Each follows a power law $Mf = A \tilde{\Lambda}^p$ within its class. Writing the pair (A, p) with A in units of $10^4 M_\odot \text{ Hz}$, the NSs give $(2.2, -0.307)$, $(4.1, -0.313)$, and $(3.7, -0.262)$ for f_{cut} , f_{merger} , and f_2 , and the SSs give $(1.5, -0.272)$, $(3.4, -0.292)$, and $(4.4, -0.296)$. The exponents agree between the classes to within ~ 0.04 but with different amplitudes. The residual scatter about the fits is at most 2.2%.

At fixed $\tilde{\Lambda}$ the equal-mass SS binaries sit up to $\sim 12\%$ above the NS f_{cut} relation, well beyond the 2.2% residual scatter—a genuine class difference set by the self-bound nature and smaller radii of SSs. Their f_2 , however, lies $\sim 13\text{--}22\%$ below, a much larger and oppositely signed shift. This shift is dynamical rather than structural. The violent radial bounce and shock re-expansion at merger lower the average density of the oscillating remnant, so f_2 falls even though the SS is the more compact star before merger. These offsets largely persist at unequal mass. The cutoff frequency, fixed during the inspiral, stays on the relations at any mass ratio.

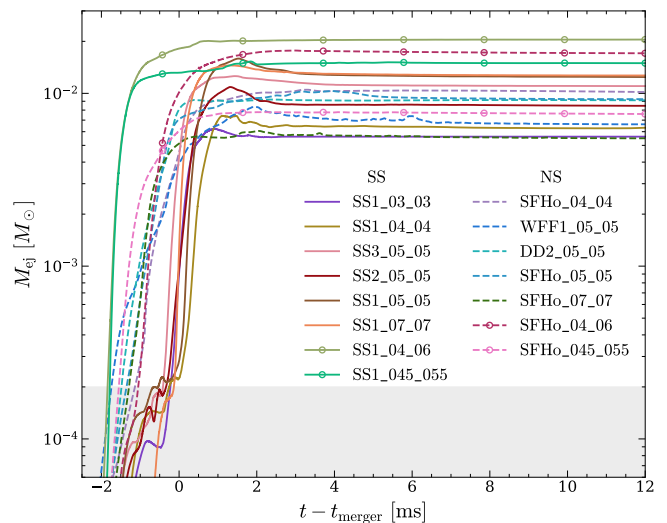


FIG. 4. Ejecta mass M_{ej} as a function of time relative to merger, for the SS (solid) and NS (dashed) binaries, computed from the Bernoulli criterion ($-hu_t > 1$). Open circles mark the unequal-mass runs ($q = 1.22$ and 1.50). Each curve uses the highest-resolution run of the binary. The shaded band ($M_{\text{ej}} < 2 \times 10^{-4} M_\odot$) marks the level of the baryonic mass-conservation error, below which the measured ejecta is not reliable. This upper bound is reached only by the unequal-mass SS binaries, while for all other runs the conservation error stays below $\sim 10^{-5} M_\odot$.

The merger frequency, by contrast, is sensitive to the tidal disruption of the lighter star at contact. For the extended NSs it falls $\sim 15\%$ below the relation at $q = 1.22$ and $\sim 31\%$ at $q = 1.5$, whereas the more compact SSs deviate by only $\sim 2\text{--}10\%$. The post-merger f_2 likewise separates the classes, except for the $q = 1.5$ SS, where the strong tidal field disrupts the companion at merger and the radial bounce is weak, so f_2 rises onto the NS relation—an extreme and isolated case.

Because f_{cut} is offset upward and f_2 downward for SSs, the two shifts compound in the ratio f_2/f_{cut} (lower panel of Fig. 3). It clusters at 2.11–2.34 for the equal-mass and $q = 1.22$ SSs and at 2.65–2.97 for the NSs. Even the extreme $q = 1.5$ SS, at 2.48, stays below the NS minimum, so the two classes do not overlap across the numerical models. We therefore expect f_2/f_{cut} to be a robust discriminant between self-bound and gravitationally bound subsolar stars. For that marginal $q = 1.5$ SS case, the merger frequency provides an independent check. Because the more compact SS resists tidal disruption until close to contact, its f_{merger} departs from the universal relation by only $\approx 10\%$, whereas the extended NS, disrupted well before contact, falls $\approx 31\%$ below it.

Ejecta.—In both classes the ejecta mainly originates in the tidal tail raised around merger, but the mechanism that unbinds it differs. Fig. 4 shows the dynamical ejecta rest mass M_{ej} , measured with the Bernoulli criterion $-hu_t > 1$ (see Table S1 for the geodesic criterion $-u_t > 1$), for all the models. Because the NS is more extended and has a larger tidal deformability, it sheds matter through spiral arms that become unbound already before merger. The far more com-

compact SS unbinds matter at merger, when the violent shock re-expansion of the merged core raises spiral arms and injects energy and angular momentum into them, producing the step-like, post-merger rise of M_{ej} . Most configurations settle to $M_{\text{ej}} \sim 10^{-2} M_{\odot}$ within ~ 10 ms of merger. The average velocity of the dynamical ejecta is in the range of $0.12\text{--}0.17c$.

Since the unbinding mechanism differs, the two classes respond oppositely as the binary is made lighter and more deformable. Along the SFHo equal-mass sequence, M_{ej} rises from $5.5 \times 10^{-3} M_{\odot}$ at a total mass of $1.4 M_{\odot}$ to $1.0 \times 10^{-2} M_{\odot}$ at $0.8 M_{\odot}$, as the lighter NS becomes more deformable and sheds a stronger tidal tail. Along the SS1 sequence it instead falls, from $1.3 \times 10^{-2} M_{\odot}$ at $1.4 M_{\odot}$ to $6.3 \times 10^{-3} M_{\odot}$ at $0.8 M_{\odot}$ and $5.6 \times 10^{-3} M_{\odot}$ at $0.6 M_{\odot}$, as the lighter, less compact SS drives a weaker collision and weaker shock re-expansion, tempering the mass ejection. In the unequal-mass binaries of both classes ($q = 1.22$ and 1.5) the heavier companion raises a massive tidal tail that begins ejecting before merger and dominates the ejecta budget, reaching the largest masses in the grid, up to $\sim 2 \times 10^{-2} M_{\odot}$. The differentially rotating remnant and its disk can unbind a further, substantial amount of mass through disk outflows on longer timescales [47, 89–94], adding to the total ejecta budget.

The subsolar BNS ejecta is expected to be neutron-rich, powering a bright kilonova (e.g., [92, 95]) whose non-detection would argue against a subsolar BNS. The SS ejecta is instead decompressed strange quark matter that may fragment into hot strangelets. Whether these evaporate into neutron-rich nucleons, driving an r -process and a kilonova much as the NS does, or survive as bound, electromagnetically dark quark nuggets is mainly set by the binding energy of quark matter at zero pressure and by the ejecta temperature [96–99].

The merger leaves a rapidly rotating remnant with a rotational energy of $\sim 10^{52}$ erg, and it likely acquires a large magnetic field [79, 94, 100, 101]. Such a field would spin the remnant down through magnetic-dipole radiation, injecting a sizable fraction of this energy into the surrounding ejecta. The energized ejecta then drives a strong shock into the interstellar medium, producing synchrotron emission from radio to X-ray wavelengths [102–104]. In addition to GWs and a kilonova, this transient would provide a further means to test the existence of subsolar-mass SS and NS mergers.

Acknowledgments—We thank the members of the Computational Relativistic Astrophysics group in AEI for helpful discussions. Numerical computations were performed on the clusters Sakura, Raven, and Viper at the Max Planck Computing and Data Facility. This work was in part supported by Grant-in-Aid for Scientific Research (grant Nos. 23H04900, 23H01172 23H01169, and 23K25869) of Japanese MEXT/JSPS, the JST FOREST Program (JP-MJFR2136), the National Natural Science Foundation of China under Grants No. 12233011, the Project for Young Scientists in Basic Research (Grant No. YSBR-088) of the Chinese Academy of Sciences.

* yong.gao@aei.mpg.de

- [1] LIGO Scientific, Virgo, and KAGRA Collaborations, arXiv e-print (2026), [arXiv:2605.27225 \[gr-qc\]](https://arxiv.org/abs/2605.27225).
- [2] A. G. Abac *et al.* (LIGO Scientific, VIRGO, KAGRA), (2025), [arXiv:2508.18082 \[gr-qc\]](https://arxiv.org/abs/2508.18082).
- [3] B. P. Abbott *et al.* (LIGO Scientific, Virgo), *Phys. Rev. Lett.* **119**, 161101 (2017), [arXiv:1710.05832 \[gr-qc\]](https://arxiv.org/abs/1710.05832).
- [4] B. P. Abbott *et al.*, *Astrophys. J. Lett.* **848**, L12 (2017), [arXiv:1710.05833 \[astro-ph.HE\]](https://arxiv.org/abs/1710.05833).
- [5] R. Abbott *et al.* (LIGO Scientific, KAGRA, VIRGO), *Astrophys. J. Lett.* **915**, L5 (2021), [arXiv:2106.15163 \[astro-ph.HE\]](https://arxiv.org/abs/2106.15163).
- [6] A. G. Abac *et al.* (LIGO Scientific, KAGRA, VIRGO), *Astrophys. J. Lett.* **970**, L34 (2024), [arXiv:2404.04248 \[astro-ph.HE\]](https://arxiv.org/abs/2404.04248).
- [7] R. Abbott *et al.* (LIGO Scientific, VIRGO, KAGRA), *Phys. Rev. X* **13**, 041039 (2023), [arXiv:2111.03606 \[gr-qc\]](https://arxiv.org/abs/2111.03606).
- [8] A. H. Nitz and Y.-F. Wang, *Phys. Rev. D* **106**, 023024 (2022), [arXiv:2202.11024 \[astro-ph.HE\]](https://arxiv.org/abs/2202.11024).
- [9] K. Kacanja, K. Soni, A. Akyüz, and A. H. Nitz, arXiv e-print (2026), [arXiv:2602.12115 \[astro-ph.HE\]](https://arxiv.org/abs/2602.12115).
- [10] A. G. Abac *et al.* (LIGO Scientific, VIRGO, KAGRA), arXiv e-print (2026), [arXiv:2605.05444 \[astro-ph.HE\]](https://arxiv.org/abs/2605.05444).
- [11] W. Niu *et al.*, arXiv e-print (2025), [arXiv:2509.09741 \[astro-ph.HE\]](https://arxiv.org/abs/2509.09741).
- [12] LIGO Scientific Collaboration, Virgo Collaboration, and KAGRA Collaboration, “GraceDB superevent S250818k,” (2025), <https://gracedb.ligo.org/superevents/S250818k/>.
- [13] LIGO Scientific Collaboration, Virgo Collaboration, and KAGRA Collaboration, “GraceDB superevent S251112cm,” (2025), <https://gracedb.ligo.org/superevents/S251112cm/>.
- [14] M. M. Kasliwal *et al.*, *Astrophys. J. Lett.* **995**, L59 (2025), [arXiv:2510.23732 \[astro-ph.HE\]](https://arxiv.org/abs/2510.23732).
- [15] X. J. Hall *et al.*, arXiv e-print (2025), [arXiv:2510.24620 \[astro-ph.HE\]](https://arxiv.org/abs/2510.24620).
- [16] K. Ackley *et al.*, arXiv e-print (2026), [arXiv:2605.02639 \[astro-ph.HE\]](https://arxiv.org/abs/2605.02639).
- [17] Y. B. Zel’dovich and I. D. Novikov, *Soviet Astronomy* **10**, 602 (1967).
- [18] B. J. Carr and S. W. Hawking, *Mon. Not. Roy. Astron. Soc.* **168**, 399 (1974).
- [19] M. Sasaki, T. Suyama, T. Tanaka, and S. Yokoyama, *Class. Quant. Grav.* **35**, 063001 (2018), [arXiv:1801.05235 \[astro-ph.CO\]](https://arxiv.org/abs/1801.05235).
- [20] T. W. Baumgarte and S. L. Shapiro, *Phys. Rev. D* **113**, 083008 (2026), [arXiv:2601.22220 \[astro-ph.HE\]](https://arxiv.org/abs/2601.22220).
- [21] M. R. Haque, F. Iocco, and L. Visinelli, arXiv e-print (2026), [arXiv:2603.25795 \[astro-ph.CO\]](https://arxiv.org/abs/2603.25795).
- [22] F. Crescimbeni, G. Franciolini, P. Pani, and A. Riotto, *Phys. Rev. D* **109**, 124063 (2024), [arXiv:2402.18656 \[astro-ph.HE\]](https://arxiv.org/abs/2402.18656).
- [23] A. L. Miller, in *Primordial Black Holes*, edited by C. Byrnes, G. Franciolini, T. Harada, P. Pani, and M. Sasaki (Springer, 2025) [arXiv:2404.11601 \[gr-qc\]](https://arxiv.org/abs/2404.11601).
- [24] Y. Suwa, T. Yoshida, M. Shibata, H. Umeda, and K. Takahashi, *Mon. Not. Roy. Astron. Soc.* **481**, 3305 (2018), [arXiv:1808.02328 \[astro-ph.HE\]](https://arxiv.org/abs/1808.02328).
- [25] B. Müller, A. Heger, and J. Powell, *Phys. Rev. Lett.* **134**, 071403 (2025), [arXiv:2407.08407 \[astro-ph.HE\]](https://arxiv.org/abs/2407.08407).
- [26] J. G. Martinez, K. Stovall, P. C. C. Freire, J. S. Deneva, F. A.

- Janet, M. A. McLaughlin, M. Bagchi, S. D. Bates, and A. Ridolfi, *Astrophys. J.* **812**, 143 (2015), arXiv:1509.08805 [astro-ph.HE].
- [27] T. M. Tauris and H.-T. Janka, *Astrophys. J. Lett.* **886**, L20 (2019), arXiv:1909.12318 [astro-ph.SR].
- [28] V. Doroshenko, V. Suleimanov, G. Pühlhofer, and A. Santangelo, *Nature Astron.* **6**, 1444 (2022).
- [29] A. L. Piro and E. Pfahl, *Astrophys. J.* **658**, 1173 (2007), arXiv:astro-ph/0610696.
- [30] B. D. Metzger, L. Hui, and M. Cantiello, *Astrophys. J. Lett.* **971**, L34 (2024), arXiv:2407.07955 [astro-ph.HE].
- [31] Y.-X. Chen and B. D. Metzger, *Astrophys. J. Lett.* (2025), 10.3847/2041-8213/ae045d, arXiv:2508.17183 [astro-ph.HE].
- [32] J. Wu, E. R. Most, N. L. Vu, N. Deppe, L. E. Kidder, K. C. Nelli, and W. Thrope, *Astrophys. J. Lett.* **1004**, L19 (2026), arXiv:2604.26912 [astro-ph.HE].
- [33] T. Nakamura, *Prog. Theor. Phys.* **81**, 1006 (1989).
- [34] A. R. Bodmer, *Phys. Rev. D* **4**, 1601 (1971).
- [35] E. Witten, *Phys. Rev. D* **30**, 272 (1984).
- [36] E. Farhi and R. L. Jaffe, *Phys. Rev. D* **30**, 2379 (1984).
- [37] C. Alcock, E. Farhi, and A. Olinto, *Astrophys. J.* **310**, 261 (1986).
- [38] J. Shao and M. Huang, arXiv e-print (2025), arXiv:2510.06065 [hep-ph].
- [39] T. Nakamura, arXiv eprint (2002), arXiv:astro-ph/0205526.
- [40] R. X. Xu, *Mon. Not. Roy. Astron. Soc.* **356**, 359 (2005), arXiv:astro-ph/0402659.
- [41] F. Di Clemente, A. Drago, P. Char, and G. Pagliara, *Astron. Astrophys.* **678**, L1 (2023), arXiv:2207.08704 [astro-ph.SR].
- [42] <https://gravvyong.github.io/subsolar/>.
- [43] T. Hinderer, *Astrophys. J.* **677**, 1216 (2008), [Erratum: *Astrophys. J.* 697, 964 (2009)], arXiv:0711.2420 [astro-ph].
- [44] T. Damour and A. Nagar, *Phys. Rev. D* **80**, 084035 (2009), arXiv:0906.0096 [gr-qc].
- [45] L.-X. Li and B. Paczynski, *Astrophys. J. Lett.* **507**, L59 (1998), arXiv:astro-ph/9807272.
- [46] B. D. Metzger, G. Martinez-Pinedo, S. Darbha, E. Quataert, A. Arcones, D. Kasen, R. Thomas, P. Nugent, I. V. Panov, and N. T. Zinner, *Mon. Not. Roy. Astron. Soc.* **406**, 2650 (2010), arXiv:1001.5029 [astro-ph.HE].
- [47] M. Shibata and K. Hotokezaka, *Ann. Rev. Nucl. Part. Sci.* **69**, 41 (2019), arXiv:1908.02350 [astro-ph.HE].
- [48] B. D. Metzger, *Living Rev. Rel.* **23**, 1 (2020), arXiv:1910.01617 [astro-ph.HE].
- [49] E. E. Flanagan and T. Hinderer, *Phys. Rev. D* **77**, 021502 (2008), arXiv:0709.1915 [astro-ph].
- [50] M. Favata, *Phys. Rev. Lett.* **112**, 101101 (2014), arXiv:1310.8288 [gr-qc].
- [51] L. Wade, J. D. E. Creighton, E. Ochsner, B. D. Lackey, B. F. Farr, T. B. Littenberg, and V. Raymond, *Phys. Rev. D* **89**, 103012 (2014), arXiv:1402.5156 [gr-qc].
- [52] J. S. Read, L. Baiotti, J. D. E. Creighton, J. L. Friedman, B. Giacomazzo, K. Kyutoku, C. Markakis, L. Rezzolla, M. Shibata, and K. Taniguchi, *Phys. Rev. D* **88**, 044042 (2013), arXiv:1306.4065 [gr-qc].
- [53] K. Hotokezaka, K. Kyutoku, Y.-i. Sekiguchi, and M. Shibata, *Phys. Rev. D* **93**, 064082 (2016), arXiv:1603.01286 [gr-qc].
- [54] K. Hotokezaka, K. Kyutoku, and M. Shibata, *Phys. Rev. D* **87**, 044001 (2013), arXiv:1301.3555 [gr-qc].
- [55] T. Hinderer, B. D. Lackey, R. N. Lang, and J. S. Read, *Phys. Rev. D* **81**, 123016 (2010), arXiv:0911.3535 [astro-ph.HE].
- [56] H. O. Silva, H. Sotani, and E. Berti, *Mon. Not. Roy. Astron. Soc.* **459**, 4378 (2016), arXiv:1601.03407 [astro-ph.HE].
- [57] Y. Gao, X.-Y. Lai, L. Shao, and R.-X. Xu, *Mon. Not. Roy. Astron. Soc.* **509**, 2758 (2021), arXiv:2109.13234 [gr-qc].
- [58] A. Bandopadhyay, B. Reed, S. Padamata, E. Leon, C. J. Horowitz, D. A. Brown, D. Radice, F. J. Fattoyev, and J. Piekarewicz, *Phys. Rev. D* **107**, 103012 (2023), arXiv:2212.03855 [astro-ph.HE].
- [59] M. Corman, W. E. East, and J. S. Read, arXiv e-print (2026), arXiv:2603.25102 [astro-ph.HE].
- [60] F. Crescimbeni, G. Franciolini, P. Pani, and M. Vaglio, *Phys. Rev. D* **111**, 083538 (2025), arXiv:2408.14287 [astro-ph.HE].
- [61] Z. Wang, Y. Gao, D. Liang, J. Zhao, and L. Shao, *JCAP* **11**, 038 (2024), arXiv:2409.11103 [astro-ph.HE].
- [62] A. Bauswein, R. Oechslin, and H. T. Janka, *Phys. Rev. D* **81**, 024012 (2010), arXiv:0910.5169 [astro-ph.SR].
- [63] E. Zhou, K. Kiuchi, M. Shibata, A. Tsokaros, and K. Uryu, *Phys. Rev. D* **106**, 103030 (2022), arXiv:2111.00958 [astro-ph.HE].
- [64] Z. Zhu and L. Rezzolla, *Phys. Rev. D* **104**, 083004 (2021), arXiv:2102.07721 [astro-ph.HE].
- [65] F. Grippa, A. Prakash, D. Logoteta, D. Radice, and I. Bombaci, *Phys. Rev. D* **111**, 083009 (2025), arXiv:2407.11143 [astro-ph.HE].
- [66] E. Zhou, K. Kiuchi, M. Shibata, A. Tsokaros, and K. Uryu, *Phys. Rev. D* **103**, 123011 (2021), arXiv:2105.07498 [gr-qc].
- [67] K. Chen and L.-M. Lin, *Phys. Rev. D* **108**, 064007 (2023), arXiv:2307.01598 [gr-qc].
- [68] C. Zhang and R. B. Mann, *Phys. Rev. D* **103**, 063018 (2021), arXiv:2009.07182 [astro-ph.HE].
- [69] L. J. Papenfort, S. D. Tootle, P. Grandclément, E. R. Most, and L. Rezzolla, *Phys. Rev. D* **104**, 024057 (2021), arXiv:2103.09911 [gr-qc].
- [70] M.-Z. Han, K. Kiuchi, and M. Shibata, (2026), in preparation.
- [71] T. Yamamoto, M. Shibata, and K. Taniguchi, *Phys. Rev. D* **78**, 064054 (2008), arXiv:0806.4007 [gr-qc].
- [72] K. Kiuchi, K. Kawaguchi, K. Kyutoku, Y. Sekiguchi, M. Shibata, and K. Taniguchi, *Phys. Rev. D* **96**, 084060 (2017), arXiv:1708.08926 [astro-ph.HE].
- [73] K. Kiuchi, L. E. Held, Y. Sekiguchi, and M. Shibata, *Phys. Rev. D* **106**, 124041 (2022), arXiv:2205.04487 [astro-ph.HE].
- [74] M. Shibata and T. Nakamura, *Phys. Rev. D* **52**, 5428 (1995).
- [75] T. W. Baumgarte and S. L. Shapiro, *Phys. Rev. D* **59**, 024007 (1998), arXiv:gr-qc/9810065.
- [76] J. G. Baker, J. Centrella, D.-I. Choi, M. Koppitz, and J. van Meter, *Phys. Rev. Lett.* **96**, 111102 (2006), arXiv:gr-qc/0511103.
- [77] M. Campanelli, C. O. Lousto, P. Marronetti, and Y. Zlochower, *Phys. Rev. Lett.* **96**, 111101 (2006), arXiv:gr-qc/0511048.
- [78] D. Hilditch, S. Bernuzzi, M. Thierfelder, Z. Cao, W. Tichy, and B. Bruegmann, *Phys. Rev. D* **88**, 084057 (2013), arXiv:1212.2901 [gr-qc].
- [79] K. Kiuchi, A. Reboul-Salze, Y. Sekiguchi, and M. Shibata, “A magnetar formation in binary neutron star merger,” (2026), arXiv:2606.11299 [astro-ph.HE].
- [80] K. Kiuchi, Y. Sekiguchi, M. Shibata, and K. Taniguchi, *Phys. Rev. Lett.* **104**, 141101 (2010), arXiv:1002.2689 [astro-ph.HE].
- [81] F. Limousin, D. Gondek-Rosinska, and E.ourgoulhon, *Phys. Rev. D* **71**, 064012 (2005), arXiv:gr-qc/0411127.
- [82] D. Gondek-Rosinska and F. Limousin, (2008), arXiv:0801.4829 [gr-qc].
- [83] J. L. Friedman, K. Uryu, and M. Shibata, *Phys. Rev. D* **65**, 064035 (2002), [Erratum: *Phys. Rev. D* 70, 129904 (2004)], arXiv:gr-qc/0108070.
- [84] A. Bauswein, N.-U. F. Bastian, D. B. Blaschke, K. Chatziioan-

- nou, J. A. Clark, T. Fischer, and M. Oertel, *Phys. Rev. Lett.* **122**, 061102 (2019), arXiv:1809.01116 [astro-ph.HE].
- [85] L. R. Weih, M. Hanauske, and L. Rezzolla, *Phys. Rev. Lett.* **124**, 171103 (2020), arXiv:1912.09340 [gr-qc].
- [86] E. R. Most, L. J. Papenfort, V. Dexheimer, M. Hanauske, S. Schramm, H. Stöcker, and L. Rezzolla, *Phys. Rev. Lett.* **122**, 061101 (2019), arXiv:1807.03684 [astro-ph.HE].
- [87] A. T.-L. Lam, Y. Gao, H.-J. Kuan, M. Shibata, K. Van Aelst, and K. Kiuchi, *Phys. Rev. Lett.* **134**, 151402 (2025), arXiv:2410.00137 [astro-ph.HE].
- [88] K. Kiuchi, K. Kawaguchi, K. Kyutoku, Y. Sekiguchi, and M. Shibata, *Phys. Rev. D* **101**, 084006 (2020), arXiv:1907.03790 [astro-ph.HE].
- [89] B. D. Metzger and R. Fernández, *Mon. Not. Roy. Astron. Soc.* **441**, 3444 (2014), arXiv:1402.4803 [astro-ph.HE].
- [90] S. Fujibayashi, K. Kiuchi, N. Nishimura, Y. Sekiguchi, and M. Shibata, *Astrophys. J.* **860**, 64 (2018), arXiv:1711.02093 [astro-ph.HE].
- [91] D. M. Siegel and B. D. Metzger, *Phys. Rev. Lett.* **119**, 231102 (2017), arXiv:1705.05473 [astro-ph.HE].
- [92] S. Fujibayashi, S. Wanajo, K. Kiuchi, K. Kyutoku, Y. Sekiguchi, and M. Shibata, *Astrophys. J.* **901**, 122 (2020), arXiv:2007.00474 [astro-ph.HE].
- [93] K. Kiuchi, S. Fujibayashi, K. Hayashi, K. Kyutoku, Y. Sekiguchi, and M. Shibata, *Phys. Rev. Lett.* **131**, 011401 (2023), arXiv:2211.07637 [astro-ph.HE].
- [94] K. Kiuchi, A. Reboul-Salze, M. Shibata, and Y. Sekiguchi, *Nature Astron.* **8**, 298 (2024), arXiv:2306.15721 [astro-ph.HE].
- [95] K. Kawaguchi, M. Shibata, and M. Tanaka, *Astrophys. J.* **889**, 171 (2020), arXiv:1908.05815 [astro-ph.HE].
- [96] C. Alcock and E. Farhi, *Phys. Rev. D* **32**, 1273 (1985).
- [97] J. Madsen, *Lect. Notes Phys.* **516**, 162 (1999), arXiv:astro-ph/9809032.
- [98] N. Bucciantini, A. Drago, G. Pagliara, S. Traversi, and A. Bauswein, *Phys. Rev. D* **106**, 103032 (2022), arXiv:1908.02501 [astro-ph.HE].
- [99] Z. Miao, Z. Zhu, and D. Lai, *Phys. Rev. Lett.* **135**, 091402 (2025), arXiv:2411.09013 [astro-ph.HE].
- [100] D. Price and S. Rosswog, *Science* **312**, 719 (2006), arXiv:astro-ph/0603845 [astro-ph].
- [101] K. Kiuchi, P. Cerdá-Durán, K. Kyutoku, Y. Sekiguchi, and M. Shibata, *Phys. Rev. D* **92**, 124034 (2015), arXiv:1509.09205 [astro-ph.HE].
- [102] B. D. Metzger and A. L. Piro, *Mon. Not. Roy. Astron. Soc.* **439**, 3916 (2014), arXiv:1311.1519 [astro-ph.HE].
- [103] K. Hotokezaka and T. Piran, *Mon. Not. Roy. Astron. Soc.* **450**, 1430 (2015), arXiv:1501.01986 [astro-ph.HE].
- [104] A. Horesh, K. Hotokezaka, T. Piran, E. Nakar, and P. Hancock, *Astrophys. J. Lett.* **819**, L22 (2016), arXiv:1601.01692 [astro-ph.HE].
- [105] E.-P. Zhou, X. Zhou, and A. Li, *Phys. Rev. D* **97**, 083015 (2018), arXiv:1711.04312 [astro-ph.HE].
- [106] M. Alford, M. Braby, M. W. Paris, and S. Reddy, *Astrophys. J.* **629**, 969 (2005), arXiv:nucl-th/0411016.

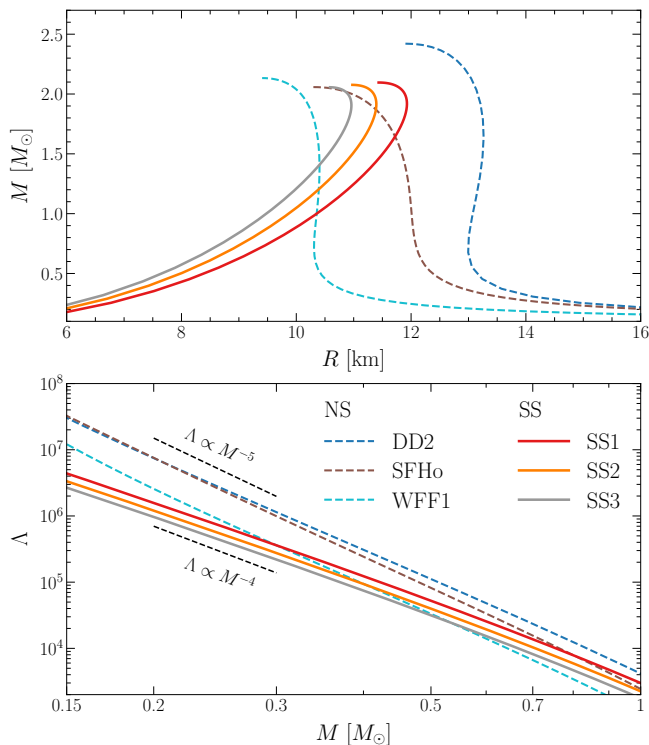


FIG. S1. Mass–radius relation (top) and dimensionless tidal deformability Λ versus mass (bottom) for the SS EOSs SS1, SS2, SS3 (solid) and the NS EOSs SFHo, WFF1, DD2 (dashed), shown down to $0.15 M_\odot$. At a fixed subsolar mass the SSs are more compact than the NSs, with correspondingly smaller tidal deformabilities.

SUPPLEMENTAL MATERIAL

Equations of state and equilibrium properties

For the SSs we adopt the unified interacting quark-matter EOS of the modified MIT bag model [68], which describes cold, charge-neutral, β -equilibrated three-flavor quark matter through

$$p = \frac{1}{3}(\epsilon - 4B) + \frac{4\lambda^2}{9\pi^2} \left[\sqrt{1 + \frac{3\pi^2(\epsilon - B)}{\lambda^2}} - 1 \right], \quad (\text{S1})$$

where ϵ is the energy density, B the effective bag constant, and λ^2 a coupling parameter that absorbs the leading perturbative-QCD correction, the strange-quark mass, and color-superconducting pairing [68, 105, 106]. The pair (B, λ^2) fixes the EOS, and the matter is self-bound: ϵ stays finite as $p \rightarrow 0$, so each star ends in a sharp surface whose density is set by B . We evolve three models, SS1, SS2, and SS3, with $(B, \lambda^2) = (52.4, 0)$, $(75.0, 38.9)$, and $(96.0, 157.3) \text{ MeV fm}^{-3}$. Larger B raises the surface density and larger λ^2 stiffens the EOS, so the stars become more compact from SS1 to SS3, with smaller tidal deformability at fixed mass. For the NSs we use three nuclear EOSs spanning the range from stiff to soft: DD2 (stiff), SFHo, and WFF1 (soft).

Fig. S1 shows the resulting stellar models, whose tidal deformabilities separate the two classes most clearly through the slope of $\Lambda(M)$. Writing $\Lambda = \frac{2}{3}k_2 C^{-5}$ with k_2 the quadrupole Love number and $C = M/R$ the compactness, the logarithmic slope decomposes as

$$\frac{d \ln \Lambda}{d \ln M} = 5 \frac{d \ln R}{d \ln M} - 5 + \frac{d \ln k_2}{d \ln M}. \quad (\text{S2})$$

The -5 from $\Lambda \propto C^{-5}$ is common to both classes, so the radius term is what distinguishes them. At low mass a self-bound SS behaves as a nearly incompressible drop with $R \propto M^{1/3}$ (Fig. S1), contributing $+5/3$. With $d \ln k_2 / d \ln M \approx -0.5$ this gives $d \ln \Lambda / d \ln M \approx -3.9$ over 0.3 – $0.7 M_\odot$, almost identical for SS1–SS3. A gravitationally bound NS instead keeps a slightly growing radius toward lower mass ($d \ln R / d \ln M \approx -0.05$ to -0.1), so the radius term nearly cancels and the slope steepens to ≈ -4.6 (DD2) and -4.9 (SFHo).

Initial parameters and merger outputs

TABLE S1. Initial parameters and merger outputs for all numerical models. For each model we list the component masses (m_1+m_2), circumferential radii (R_1, R_2), and mass-weighted tidal deformability $\tilde{\Lambda}$ (Eq. (1)), followed by the results at up to three grid resolutions, labelled by the finest grid spacing Δx_{finest} . The cutoff, peak, and post-merger frequencies $f_{\text{cut}}, f_{\text{merger}}, f_2$ are defined in the main text. The dynamical ejecta rest mass M_{ej} and mass-averaged velocity $\langle v \rangle_{\text{ej}} = \sqrt{2T/M_{\text{ej}}}$, with kinetic energy $T = E - U - M_{\text{ej}}$ (E and U the total and internal energy of the unbound matter), are evaluated 10 ms after merger, with both the geodesic criterion ($-u_t > 1$) and the Bernoulli criterion ($-hu_t > 1$).

Model	$m_1+m_2 [M_\odot]$	R_1, R_2 [km]	$\tilde{\Lambda}$	Δx_{finest} [m]	f_{cut} [Hz]	f_{merger} [Hz]	f_2 [Hz]	Geodesic		Bernoulli	
								$M_{\text{ej}} [10^{-2}M_\odot]$	$\langle v \rangle_{\text{ej}} [c]$	$M_{\text{ej}} [10^{-2}M_\odot]$	$\langle v \rangle_{\text{ej}} [c]$
SS1	0.3+0.3	7.1	3.6×10^5	184.6	798.3	1331.5	1666.4	0.07	0.111	0.15	0.094
				138.4	798.3	1350.9	1666.6	0.39	0.123	0.43	0.120
				110.7	787.7	1365.8	1665.1	0.40	0.132	0.56	0.130
SS1	0.4+0.4	7.8	1.2×10^5	197.0	780.6	1356.8	1749.8	0.30	0.121	0.36	0.116
				148.0	777.8	1379.5	1785.0	0.12	0.118	0.15	0.111
				118.1	779.0	1376.8	1694.0	0.54	0.128	0.63	0.123
SS1	0.45+0.55	8.1, 8.7	5.2×10^4	246.0	782.1	1372.6	1733.0	1.42	0.166	1.45	0.165
				184.6	782.1	1386.7	1799.7	1.31	0.163	1.34	0.162
				147.7	782.1	1404.3	1799.8	1.45	0.161	1.50	0.160
SS1	0.5+0.5	8.4	5.2×10^4	221.5	806.8	1431.7	1774.9	0.40	0.147	0.45	0.142
				166.1	796.5	1438.6	1724.9	1.27	0.152	1.38	0.148
				132.9	825.0	1447.0	1743.0	1.14	0.147	1.25	0.143
SS1	0.4+0.6	7.8, 8.9	5.2×10^4	184.6	795.2	1281.1	2066.4	2.03	0.160	2.09	0.158
				147.7	804.9	1296.7	2066.4	1.88	0.163	1.93	0.161
				123.0	818.2	1300.3	2032.2	1.99	0.161	2.05	0.159
SS1	0.7+0.7	9.3	1.4×10^4	246.1	827.6	1482.3	1866.4	0.54	0.174	0.58	0.171
				184.6	827.6	1502.1	1866.4	1.19	0.168	1.26	0.166
				147.7	807.7	1509.5	1891.6	1.21	0.167	1.27	0.164
SS2	0.5+0.5	8.0	4.0×10^4	204.3	865.2	1522.9	1916.4	1.02	0.154	1.10	0.151
				153.2	868.7	1569.3	1853.7	1.24	0.150	1.35	0.147
				122.6	865.2	1566.4	1916.6	0.76	0.144	0.85	0.140
SS3	0.5+0.5	7.7	3.2×10^4	196.9	910.8	1649.0	1999.8	0.79	0.160	0.85	0.156
				147.7	920.2	1678.0	1999.7	1.06	0.156	1.14	0.153
				118.1	928.5	1664.6	1999.9	1.04	0.148	1.10	0.146
SFHo	0.4+0.4	12.7	2.4×10^5	270.7	570.0	941.5	1699.8	1.12	0.129	1.03	0.132
				203.0	592.1	1042.2	1749.9	1.00	0.110	0.88	0.113
				162.4	601.1	1048.4	1784.1	1.15	0.114	1.03	0.116
SFHo	0.45+0.55	12.5, 12.3	8.3×10^4	246.1	647.5	989.3	1883.8	1.14	0.150	1.05	0.154
				184.6	668.0	1014.1	1949.9	1.05	0.148	0.97	0.152
				147.7	666.2	1017.4	1849.8	0.83	0.153	0.76	0.157
SFHo	0.5+0.5	12.4	8.2×10^4	246.1	663.3	1141.8	1933.1	0.81	0.124	0.72	0.128
				184.6	675.8	1176.2	1888.7	0.90	0.133	0.82	0.136
				147.7	681.0	1183.0	1909.0	1.00	0.137	0.93	0.139
SFHo	0.4+0.6	12.7, 12.2	8.7×10^4	246.1	636.4	820.3	1799.8	1.94	0.169	1.86	0.171
				184.6	643.1	834.1	1799.8	1.80	0.171	1.73	0.173
				147.7	624.0	818.3	1737.0	1.78	0.173	1.71	0.175
SFHo	0.7+0.7	12.1	1.6×10^4	184.6	782.2	1393.6	2066.4	0.53	0.145	0.47	0.149
				147.7	794.3	1418.3	2219.1	0.40	0.145	0.35	0.151
				123.0	797.0	1417.6	2133.3	0.60	0.151	0.55	0.155
WFF1	0.5+0.5	10.4	3.3×10^4	246.1	849.3	1490.1	2266.4	0.23	0.112	0.32	0.106
				184.6	872.5	1595.9	2346.5	0.22	0.116	0.29	0.110
				147.7	881.6	1620.9	2333.0	0.60	0.131	0.66	0.128
DD2	0.5+0.5	13.1	1.1×10^5	270.7	630.0	1077.3	1733.0	1.11	0.122	1.02	0.124
				203.0	619.5	1107.8	1666.5	1.35	0.131	1.26	0.134
				162.4	619.5	1124.9	1767.1	1.01	0.134	0.91	0.137

Code performance of SACRA-K

The simulations presented in this work are performed with SACRA-K on the Viper APU cluster of the Max Planck Computing and Data Facility¹. SACRA-K uses a nested Cartesian grid with 2:1 box-in-box adaptive mesh refinement and mirror symmetry about the orbital ($z = 0$) plane. The grid has ten refinement levels: each star is covered by four finer comoving domains, while six coarser domains enclose both stars and are centered on the binary’s center of mass. Each domain is a uniform cell-centered Cartesian grid of $2N \times 2N \times N$ cells in (x, y, z) , with six buffer cells on each side. The grid spacing on level ℓ is $\Delta x^{(\ell)} = L^{(\ell)} / (2N)$, where $L^{(\ell)}$ is the size of the domain in the x and y directions. Every level is split into $\text{jprocs} \times \text{kprocs} \times \text{lprocs}$ subdomains in (x, y, z) , and each MPI rank evolves one subdomain across all levels, exchanging boundary data through GPU-aware MPI. Table S2 lists the setup and measured performance for a representative binary, whose three resolutions $N = 60, 80,$ and 100 use 1, 2, and 4 nodes at ≈ 3 s per step and advance 50–106 ms of physical evolution per day.

TABLE S2. Parallel setup, per-step wall-clock time, and physical evolution covered per day for SACRA-K on the Viper APU nodes, for the representative $0.5+0.5 M_{\odot}$ SFHo binary at its three grid resolutions.

N	Δx_{finest} [m]	nodes	$\text{jprocs} \times \text{kprocs} \times \text{lprocs}$	ranks	t_{step} [s]	$t_{\text{phys/day}}$ [ms]
60	246.1	1	$2 \times 2 \times 1$	4	2.7	106
80	184.6	2	$2 \times 2 \times 1$	4	3.3	64
100	147.7	4	$4 \times 2 \times 1$	8	3.4	50

¹ <https://docs.mpcdf.mpg.de/doc/computing/viper-gpu-user-guide.html>